Table 3.6. Fundamental voltage solutions used in uncertainty analysis. Deliberate errors are underlined.

Voltage	No errors	Case 1	Case 2	Case 3
V_0	0.000000E+00	0.000000E+00	0.000000E+00	0.000000E+00
V_1	0.227477E-02	0.227477E-02	0.227477E-02	0.227477E-02
V_2	0.943045E-02	0.943045E-02	0.943045E-02	0.953045E-02
V_3	0.225976E-01	0.225976E-01	0.225976E-01	0.225976E-01
V_4	0.443181E-01	0.443181E-01	0.444181E-01	0.443181E-01
V_5	0.802967E-01	0.802967E-01	0.802967E-01	0.802967E-01
V_6	0.145450E+00	0.145550E+00	0.145450E+00	0.145450E+00
V_7	0.294655E+00	0.294655E+00	0.294655E+00	0.294655E+00
V_8	0.132742E+01	0.132742E+01	0.132742E+01	0.132742E+01

Table 3.7. Conductivity parameter values resulting from voltages in Table 3.6.

Coefficient	No errors	Case 1	Case 2	Case 3
C_0	0.10001E+01	0.99885E+00	0.10011E+01	0.99976E+00
C_1	-.26065E-03	0.70206E-02	-.38374E-02	-.32062E-03
C_2	-.79597E-03	0.16049E-01	-.14456E-01	0.15128E-02

some differences attributed to finite numerical precision still remain. Second, the errors in the conductivity parameter values in all cases are smallest for C_0, intermediate for C_1, and largest for C_2. Third, the errors decrease as the index of the voltage in which the error is introduced is decreased. These last two observations are in harmony with the concepts that the largest of the fundamental voltages are the most important in the reconstruction, and that the coefficients of the higher-degree polynomials require more of the larger voltages to be measured accurately. Fourth, the errors in case 3 are acceptably small, but the errors in cases 1 and 2 (particularly in C_2) are not. This suggests that experimental datasets should average more than 25 measurements for each projection set, the number used in early tests and experiments with the EIT system.

3.4. Selection of Electrode Geometry for Multiphase Flow Measurements

The final evaluation of strip and point electrode geometries used measurements of baseline liquid conductivities taken with each electrode array in the vertical bubble column described in the next chapter. These measurements were taken during preliminary tests of

vertical gas-liquid flows in the column, in periods of no gas flow. Fundamental voltage solutions were derived from these no-flow data with EITFUN and compared to calculated solutions from FIDAP for the appropriate electrode geometry with a uniform conductivity field in three dimensions. The comparisons gave a clear indication of the best choice for multiphase flow measurements.

The fundamental voltages from the square and circular electrode data were in poor agreement with calculated values; the experimental voltages were similar at all non-current-bearing electrodes. Besides implying a potential for significant disagreement between actual and calculated conductivity profiles, this similarity indicated that under multiphase flow conditions, the electrodes would have poor sensitivity to variations in the conductivity profile. In contrast, the fundamental voltage solutions from strip electrode data were in excellent agreement with the computational values at the non-current-bearing electrodes 0 through 7 (see Table 3.4). Although the voltages at the current-bearing electrode (V_8) differed somewhat from the fundamental solution, probably because of contact impedance, the reconstruction algorithm does not use this quantity (Torczynski *et al.*, 1996a and 1997). The voltages at non-current-bearing strip electrodes also varied significantly from one electrode to the next, implying a higher sensitivity to changes in the domain conductivity profile. Several possible explanations for the higher performance of the strip electrodes have been advanced, including their larger area compared to the square and circular electrodes (4.84 cm^2 versus 1.61 cm^2 and 1.27 cm^2, respectively); the fact that the strip electrodes more closely resemble "two-dimensional" electrodes; and the smaller fraction of the column circumference subtended by the strips compared to the squares and disks.

As seen in Table 3.4, multiplying the strip electrode experimental values by 1.007 brings them into agreement with computed voltages to almost three significant figures. A systematic difference of 0.7% between computational and experimental voltages is reasonable, since experimental uncertainty in measurements of injected current and liquid conductivity is about ±0.5% and computational accuracy is similar. Based on these results, strip electrodes were used exclusively to reconstruct the radial profiles of the multiphase flows discussed in the remainder of this report.

3.5. Summary

In this chapter the Sandia/Michigan EIT hardware and reconstruction algorithms have been presented and evaluated. The electronics used to inject current into the domain and measure voltages at the boundary have been described in detail, including improvements to reduce acquisition time. An algorithm has been implemented in two and three dimensions to reconstruct distributions of insulating phases within a continuous conducting phase, such as gas bubbles or insulating solid particles in conducting liquid. Both the two-dimensional and three-dimensional codes are capable of reconstructing uniform and radially varying conductivity distributions that are useful in the analysis of vertical bubble-column flows. The three-dimensional algorithm has recently been expanded to allow quartic radial gas volume fraction

profiles, so that EIT may be used with the same generality as the gamma-densitometry tomography method employed at Sandia.

As a validation test of the reconstruction algorithm alone, boundary voltages were computed from analytical conductivity distributions and input to the algorithm; the original conductivity distributions were accurately reproduced by the reconstruction code. Next, using a method common to many EIT studies, known geometries of insulating inclusions in a conducting domain were measured with the Sandia/Michigan EIT system and reproduced with the reconstruction codes and measured voltage data. The combination of hardware and software reproduced the volume fraction of each inclusion to within 0.006 and its position to within 3%, demonstrating the ability of the system to quantitatively measure static insulating phase distributions. An assessment of the uncertainty in the quartic reconstruction algorithm indicated that the use of higher-order coefficients requires: (1) high accuracy in the largest experimental voltages near the injection electrode, and (2) datasets that average more than the 25 measurements typically used in early EIT tests. Finally, a commercial finite-element code was used to investigate the accuracy of the Maxwell-Hewitt equations used to convert conductivity distributions to phase volume fraction distributions. It was concluded that these equations will accurately determine insulating phase volume fractions from measured conductivity data, with a small but acceptable tendency to overpredict the amount of insulating phase. With these successful validation tests, the EIT system and the Maxwell-Hewitt equations can now be applied to the measurement of insulating volume fraction distributions in vertical multiphase bubble-column flows.

4. Evaluation of the Sandia/Michigan EIT System in Two-Phase Flows

In this chapter, a series of studies is presented in which the EIT system described in Chapter 3 was applied to solid-liquid and gas-liquid two-phase flows. The Sandia/Michigan EIT system and an established gamma-densitometry tomography (GDT) system were simultaneously applied to the same flows, and the results were compared to judge the accuracy of the EIT system for two-phase flow measurements (Shollenberger *et al.*, 1997b; George *et al.*, 1998a, 1999c). The GDT system developed at Sandia has already been successfully applied to multiphase flows (Adkins *et al.*, 1996; Torczynski *et al.*, 1996b; Shollenberger *et al.*, 1995, 1997a), making it a useful validation tool.

The EIT system was applied to the task of *in situ* measurement of dispersed solid-liquid and gas-liquid flows to determine its ability to measure volume-averaged phase fractions and spatial phase distributions. In the solid-liquid tests, the size of the dispersed solid phase was much smaller than the size of the test vessel. In the gas-liquid bubbly flows, the scale of the dispersed phase (air bubbles) was larger than in the solid-liquid mixture but still small compared to the scale of the apparatus. This increase in phase scale represents a progression toward industrial-scale multiphase flows, where EIT may ultimately be applied to resolve questions about phase distributions and effects of solid phases in three-phase flows.

Liquid conductivity was controlled during the two-phase experiments by adding sodium nitrate to deionized water, ensuring that resistive effects would dominate over capacitive effects in EIT measurements as explained in Section 3.2.2. This marks a change from the validation tests in Chapter 3, where sodium chloride was used; sodium nitrate was chosen for all subsequent tests to minimize the possibility of electrode corrosion.

The governing equation for the computational domain, Eq. 3.1, assumes that no charge sources or sinks are present in the domain. For multiphase experiments, this assumption requires that no grounded conductors (except for the EIT withdrawal electrode) may be in contact with the conducting medium anywhere within 10 column diameters of the electrode ring. To enforce this requirement, only electrically isolated instruments (cartridge heaters and thermocouples) were allowed at the flow boundaries, and mechanical devices within the flows were electrically isolated or given nonconducting coatings.

The remainder of this chapter begins with a brief description of the Sandia GDT system, then continues with discussions of the experimental conditions of each two-phase flow test, the GDT and EIT results, and an assessment of EIT accuracy in each test. Unlike EIT studies involving image reconstruction – *e.g.*, Lin *et al.* (1993) – the emphasis here is not on visualization or on the accurate determination of interfaces between spatially segregated phases, but on the quantitative measurement of mixture properties for dispersed multiphase flows. The

quantities determined by both GDT and EIT are averages over length scales larger than that of the dispersed phase but smaller than the measurement domain.

4.1. The Sandia GDT System

Many tomographic methods applied to multiphase flows involve radiation, such as neutrons, gamma rays, or x-rays, that is partially attenuated by the flow. Information about local density or phase distributions can be obtained by measuring the attenuation of radiation through the domain or by triangulating the locations of radiation sources within the flow (George *et al.*, 1998a). Gamma-densitometry tomography (GDT) uses collimated radiation sources to project beams of photons through the region of interest and detection systems to measure the fraction of photons that pass through the region unattenuated. Measurement of the attenuation along many different paths through the domain can be combined with linear tomographic reconstruction methods to produce an image of the phase distribution in the domain. GDT has been used for some time to investigate multiphase flows, and Munshi (1990), Beck *et al.* (1993), and Simons (1995) provide comprehensive reviews of the technique. GDT requires that the two phases have significantly different attenuation coefficients for good image resolution or useful quantitative results.

The GDT system developed at Sandia for studies of industrial-scale multiphase flows (Torczynski *et al.*, 1996b, 1997; Shollenberger *et al.*, 1997a) is shown in Figure 4.1. Figure 4.2 shows a schematic of the traverse as viewed from above, and Figure 4.3 presents a block diagram of the complete system. The system employs a 5-curie ^{137}Cs gamma source, a sodium-iodide scintillation detector system, computer-controlled traverses to position the source and detector on opposite sides of the test object, and hardware and software for data acquisition and system control. Attenuation of the 0.662-MeV photons is measured along many parallel beam paths, then attenuation by the testbed walls is subtracted from the raw data, and a path-averaged gamma attenuation coefficient, $\hat{\mu}$, is determined for each path within the domain.

Since GDT measurements require from 15 to 30 minutes, GDT essentially yields time-averaged results. In the bubble-column flows examined in this work, checks of the GDT attenuation profiles consistently revealed side-to-side symmetry across the column diameter over this time period, which justifies the assumption of an axisymmetric phase distribution. Using this assumption, the Abel transform (Vest, 1985) is used to convert the path-averaged attenuation coefficients $\hat{\mu}$ to a time-averaged, normalized, radial attenuation distribution, $\mu(r)$, in the circular domain. The attenuation distribution must then be transformed to a phase distribution through a mathematical relationship involving the attenuation coefficients of the separate phases. For the case of gas-liquid flows, the attenuation information may be converted to a gas volume fraction profile $\varepsilon_G(r)$ through the linear formula

$$\varepsilon_G^{GDT}(r) = \frac{\mu_L - \mu(r)}{\mu_L - \mu_G}, \tag{4.1}$$

Figure 4.1. The Sandia GDT system and the transparent bubble column used in gas-liquid experiments. The ^{137}Cs source is in the foreground, shown on its traverse arm. The motor that positions the arms vertically is at top right.

where r is the radial coordinate, and μ_L and μ_G, the gamma ray attenuation coefficients of the liquid and gas, respectively, have been previously measured or are known *a priori*. The liquid volume fraction profile, $\varepsilon_L(r)$, may also be determined by subtracting the local value of $\varepsilon_G(r)$ from unity. More details on the GDT system and reconstruction algorithm may be found in Torczynski *et al.* (1997); a listing of the current version of the reconstruction code, `GDTAXI`, appears in Appendix I.

For the flows examined in this report, both the attenuation and phase distributions are modeled by the GDT reconstruction algorithm as polynomials with only even powers of r, based on the observation that the measured attenuation profiles are axisymmetric. The EIT reconstruction algorithm also assumes axisymmetric material distributions in these tests, allowing straightforward comparisons of EIT and GDT results. By substituting a cross-sectionally-averaged gamma attenuation coefficient $\langle\mu\rangle$ for $\mu(r)$ in Eq. 4.1, a cross-sectionally-averaged phase volume fraction, $\langle\varepsilon_G\rangle$, may be obtained. Also, as will be demonstrated in the

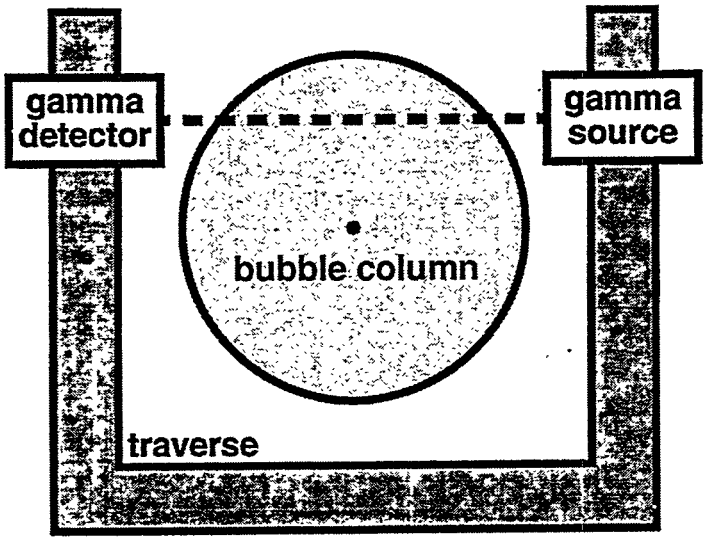

Figure 4.2. Conceptual diagram of the Sandia GDT system as viewed from above.

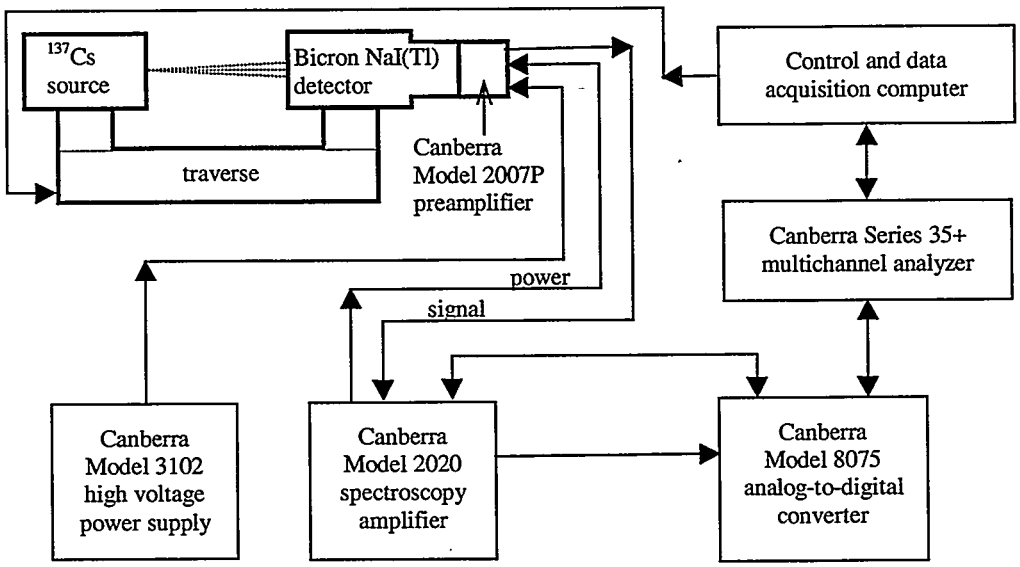

Figure 4.3. Block diagram of the Sandia GDT system.

next section, GDT data may be used with the same algorithm and a similar formula to measure phase distributions in solid-liquid or solid-gas flows if the attenuation coefficients of the two phases differ significantly (George *et al.*, 1999b).

4.2. Solid-Liquid Experiments

The first two-phase EIT validation experiments involved a closed container of conducting liquid with a flow of insulating solid particles driven by an impeller. This solid-liquid flow was chosen for two reasons. First, the amount of solids introduced into the container can be carefully controlled, providing an independent check of the tomography results. Second, unlike gas bubbles, solid particles can be small, uniform spheres that do not change shape during the experiment, so long as conditions are not harsh enough to fracture the particles. The solid particles and the liquid medium can be chosen to have significantly different gamma attenuation coefficients and electrical conductivities, so that GDT and EIT can be applied separately and independently to determine the solid volume fraction. However, liquids and insulating solids that have significantly different attenuation coefficients typically have substantially different densities as well, making the solids difficult to loft uniformly (Shollenberger *et al.*, 1997b).

A schematic diagram and a photograph of the experimental setup are shown in Figures 4.4 and 4.5. The testbed consisted of the strip-electrode cylinder stacked between two Lexan cylinders of the same inner diameter and wall thickness. This testbed, 81.3 cm in height, was found to be tall enough to encompass all the significant electric field lines from the strip electrodes. The three-part cylinder was capped at the bottom and the top, and a mixer was inserted into the cylinder through a 2.5-cm-diameter hole in the center of the top cap. The mixer consisted of a compact impeller assembly, a 1.5-watt Sargent-Welch motor (model S-76509-80B) mounted above the testbed, and a two-piece shaft 0.8 cm in diameter extending from the impeller to the motor. Since the mixer's original shaft was not long enough to reach out of the cylinder, an insulating Lexan extender joined the end of the mixer shaft to a second shaft attached to the mixer motor. The mixer was used to generate a relatively uniform solids distribution inside the cylindrical testbed. To prevent settling of the solids, the impeller was positioned 1.27 cm above the testbed floor. An overflow volume was placed around the top cap to eliminate free-surface effects — *e.g.*, a vortical "funnel" — in the cylinder interior during mixing.

Although the mixer shaft was small compared to the test cylinder (the ratio of their diameters was 0.042), the presence of the shaft posed problems for EIT. Placing an unshielded electrical conductor in the center of the testbed has the potential to significantly distort the electric field lines, so the steel shaft and impeller were coated with a layer of insulating paint to mitigate this effect. The Lexan extender also served to further insulate the motor assembly from the testbed. Earlier EIT measurements with and without the mixer shaft in place, with no particles present, verified that the insulated shaft had only a small effect on EIT measurements (Shollenberger *et al.*, 1997b).

The liquid phase was deionized water with a small amount of saturated sodium nitrate solution added for conductivity control. Liquid conductivity values ranged from 265 to 275 μS/cm over the course of experiments. For the solid phase, polystyrene spheres with a density of ρ_S = 1.04 g/cm^3 and a range of diameters from 200 to 700 μm were used (Figure 4.6). Polystyrene was chosen for this experiment because its specific gravity is nearly that of water,

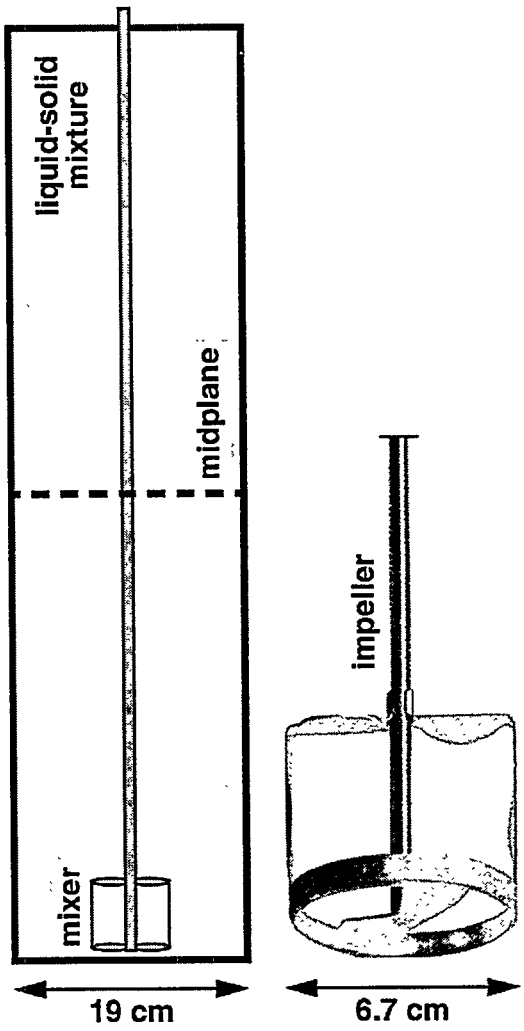

Figure 4.4. Schematic of test geometry for the solid-liquid experiments showing the impeller geometry and location within the testbed (adapted from Shollenberger *et al.*, 1997b).

making it easier to loft uniformly within the flow than heavier solids. Polystyrene is also an insulator with respect to water, so that EIT is able to discriminate between the solid and liquid phases. GDT is not useful in this case because the attenuation coefficients of polystyrene and water are too similar for the phases to be distinguished [$\mu_L = 0.0856$ cm^{-1}, $\mu_S = 0.0866$ cm^{-1} (Thoraeus, 1965)]. Instead, EIT measurements were compared to the nominal cylinder-averaged solid volume fraction $\bar{\varepsilon}_S^{NOM}$ chosen for each test.

For each chosen value of $\bar{\varepsilon}_S^{NOM}$, the appropriate mass of polystyrene was computed from its density and the volume of the test cylinder. The required mass of spheres was introduced into the testbed, and liquid was added to occupy the remaining volume. A mixer speed of 420 rpm was applied for 30 minutes to all solid loadings, with the result that a roughly uniform distribution of particles was observed visually within the liquid during measurements (Figure 4.7). EIT voltage measurements were taken periodically over the thirty-minute stirring period to

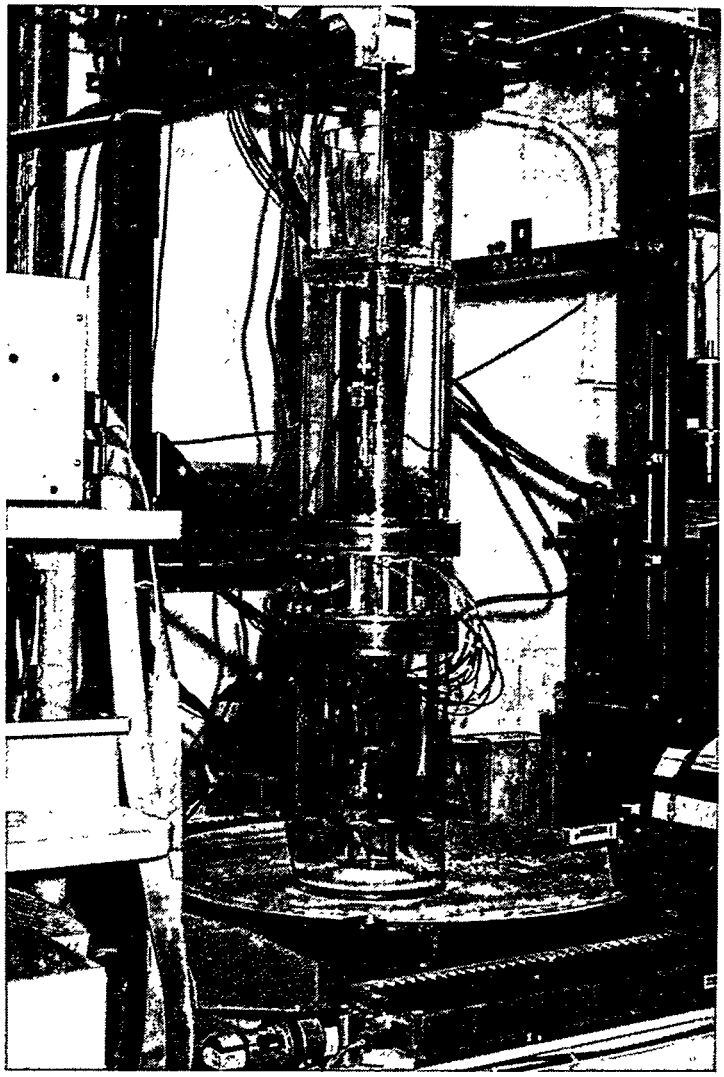

Figure 4.5. Photograph of the testbed for polystyrene-water solid-liquid experiments. The impeller motor is visible at the top; the EIT cabinet and GDT source are on the left and right sides of the photo, respectively.

verify that a steady-state distribution had been attained. After EIT measurements were taken of the uniform equilibrium distribution, mixing was terminated, the spheres were allowed to settle to the bottom of the cylinder, and EIT was applied again. The second EIT measurement was necessary to determine a baseline liquid conductivity for calibration: despite attempts to wash and rinse the polystyrene particles before the experiments, soluble contaminants were introduced with the particles that altered the conductivity of the water. The magnitude of this effect on the water conductivity was comparable to that of the suspended solid particles during mixing. By comparison, changes in water temperature and associated conductivity changes were negligible during mixing. In both the calibration measurements and the measurements of the uniform solid-liquid flow, 25 complete projection sets were averaged over a period of about 20 seconds to average out the effects of any fluctuations in the flow and thereby justify the assumption of axisymmetry in reconstructions.

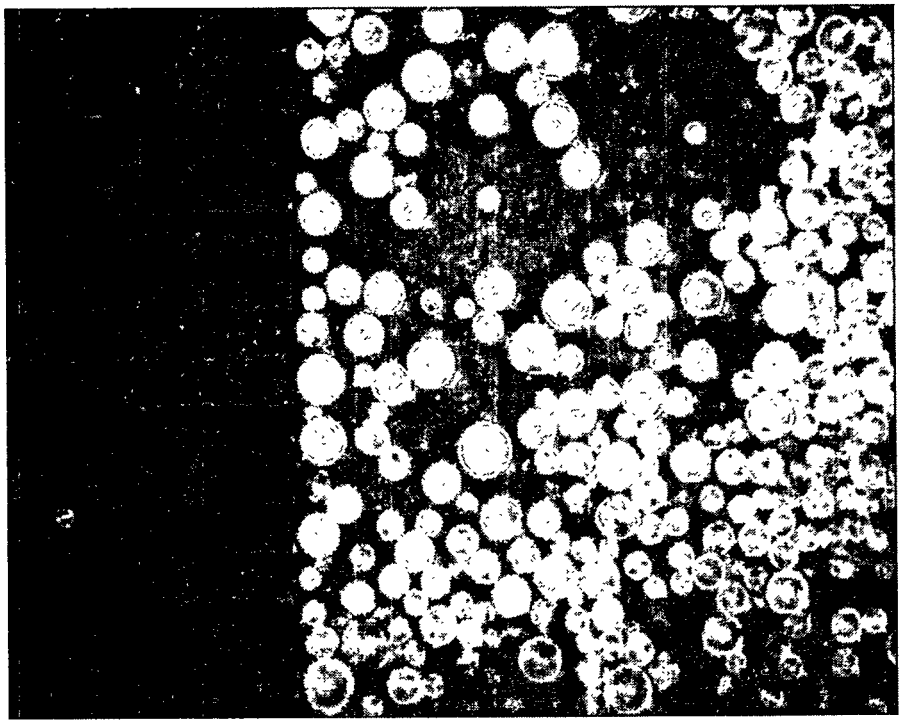

Figure 4.6. Photograph of polystyrene particles used as the solid phase. The smallest division on the scale is 0.5 mm.

Analysis of the solid-liquid data with EITAXI demonstrated that the radial solids profiles were uniform to within experimental uncertainty, as expected. Radial variations in the local solids density ε_S were less than 0.01 across the domain, changing over length scales much larger than the diameters of the particles themselves. The radial profiles were analytically integrated to obtain cross-sectionally-averaged solid volume fractions $\bar{\varepsilon}_S^{EIT}$, plotted in Figure 4.8. The solid volume fractions determined by EIT are seen to be in close agreement in all cases with the nominal values computed from the mass of added particles, validating the EIT method for solid-liquid measurements.

The difference between measured and nominal solid volume fractions becomes more negative with increasing solid volume fraction, approaching $\bar{\varepsilon}_S^{EIT} - \bar{\varepsilon}_S^{NOM} = -0.003$ when $\bar{\varepsilon}_S^{NOM} = 0.050$. It is possible that the ability of the mixer to produce a uniform axial distribution dropped with increased solid loadings, so that the local solid volume fraction was slightly lower than the nominal value near the top of the cylinder and slightly higher at the bottom. Another possible explanation for the trend stems from the observation that a small amount of solids escaped through the hole in the top cap over the course of each test. These solids passed into the overflow volume and reduced the actual amount of solids visible to EIT in the measurement volume. The fraction of total solids lost to the overflow volume was observed to increase with nominal loading, possibly causing the observed trend.

Before the validation tests in Chapter 3 were performed to determine an optimum electrode geometry, an EIT experiment was conducted by Sandia researchers in a solid-liquid

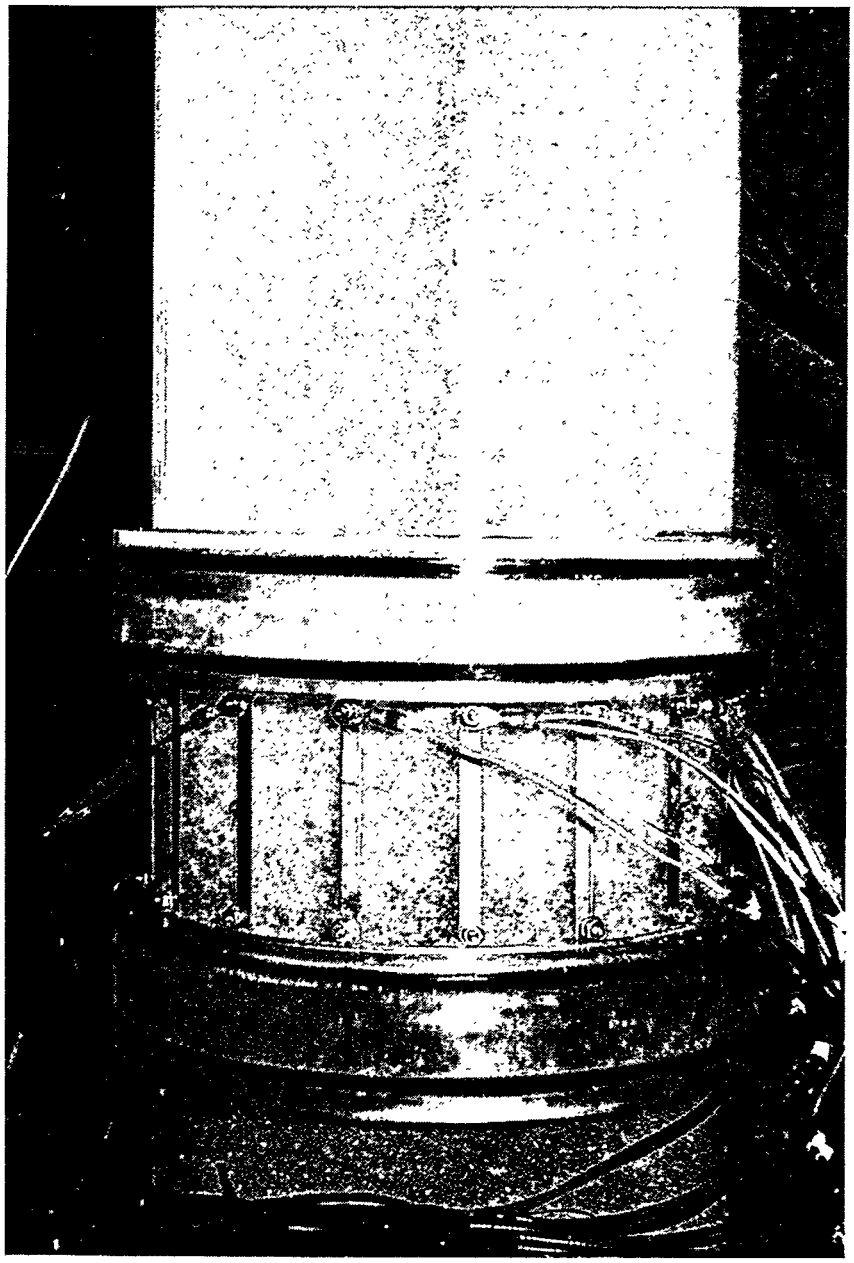

Figure 4.7. Photograph of flow conditions during solid-liquid experiments with $\bar{\varepsilon}_s^{NOM}$ = 0.01.

flow employing glass spheres with a mean diameter of 80 μm as the solid phase (Shollenberger *et al.*, 1997b). This experiment involved an electrode ring composed of sixteen disk electrodes 3 mm in diameter. Though the geometry tests later found strip electrodes to be superior to the point-like electrodes, these test results are significant because GDT was used to validate the EIT measurements. The experiments were very similar in setup and execution to the polystyrene-water experiments, but some differences should be noted, particularly the different collection times for EIT data and the higher electrical conductivity of the liquid phase required by the

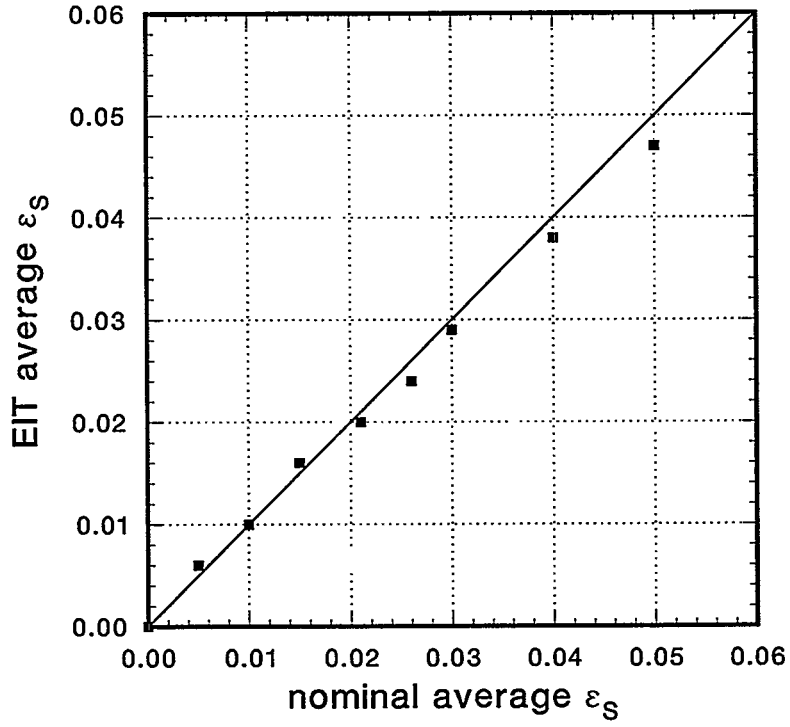

Figure 4.8. Solid volume fractions measured by EIT in polystyrene-water solid-liquid mixtures.

smaller size of the electrodes. The reader is referred to Torczynski *et al.* (1997) for details of these glass-water tests.

Analysis of the GDT glass-water data demonstrated that the time-averaged radial solids profiles were relatively uniform across the testbed. Using the assumption of a spatially uniform gamma attenuation coefficient $\langle \mu \rangle$, GDT data were converted to cross-sectionally-averaged solid volume fractions through the formula

$$\langle \varepsilon_S \rangle^{GDT} = \frac{\langle \mu \rangle - \mu_L}{\mu_S - \mu_L}, \tag{4.2}$$

where the attenuation coefficients μ_L and μ_S of the water and glass spheres were previously measured (Torczynski *et al.*, 1996b). Similarly, nearly identical domain-averaged conductivities $\overline{\sigma}$ were obtained from the EIT algorithm when using either a spatially uniform conductivity distribution or a radially parabolic distribution, so the simpler uniform distribution was employed. This simplification allowed the transformation of average EIT data directly to an average solid volume fraction, without integration of the volume fraction profile. The three-dimensional Maxwell-Hewitt relation, Eq. 3.13, was used with the solid-liquid continuity equation to arrive at the final formula,

$$\overline{\varepsilon}_S^{EIT} = \frac{1 - [\overline{\sigma}/\sigma_L]}{1 + \frac{1}{2}[\overline{\sigma}/\sigma_L]}. \tag{4.3}$$

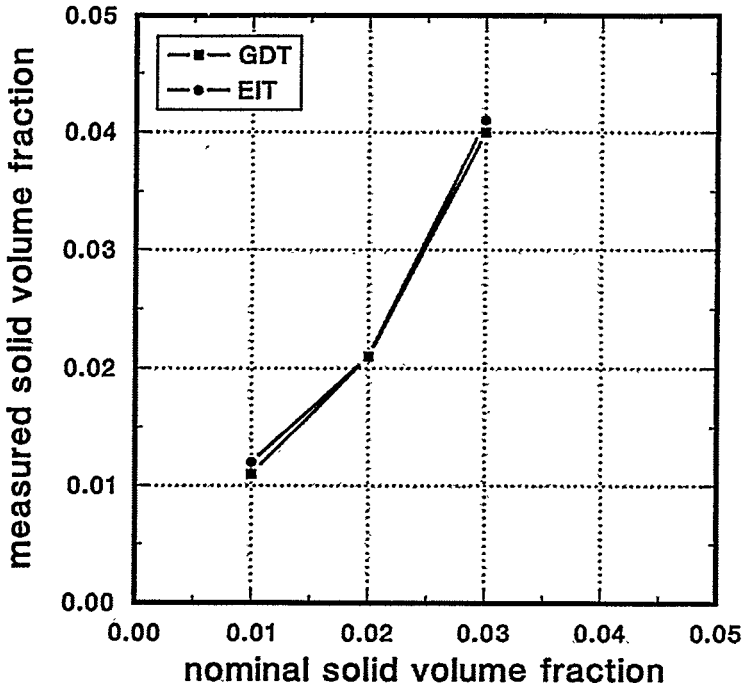

Figure 4.9. Comparison of testbed-averaged solid volume fractions measured by EIT and GDT in glass-water mixtures (from Shollenberger *et al.*, 1997b).

The solid volume fractions determined by GDT and EIT were in close agreement with each other for all three cases (Figure 4.9) and with the nominal values for the two lower solids loadings. The case of $\bar{\varepsilon}_s^{NOM} = 0.03$ is interesting in that the GDT and EIT values were in agreement with each other but were somewhat higher than the nominal value. It was conjectured (as in the polystyrene tests) that the mixing in the latter case may not have been strong enough to overcome buoyancy-driven stratification, and thus did not produce a uniform solids distribution (Shollenberger *et al.*, 1997b). However, the close agreement between GDT and EIT in all three cases further validates the Sandia/Michigan EIT system in the measurement of solid-liquid phase distributions.

4.3. Gas-Liquid Experiments

4.3.1. Experimental Setup and Conditions

In the next phase of EIT evaluation, gas volume fraction spatial distributions were measured in air-water flows with both EIT and GDT. These gas-liquid tests were conducted in a transparent Lexan bubble column assembled at Sandia as a testbed for optical, electrical, and radiation-based multiphase flow diagnostics (Torczynski *et al.*, 1997). Figure 4.10 shows the EIT and GDT systems in place around the bubble column. The column itself, also shown

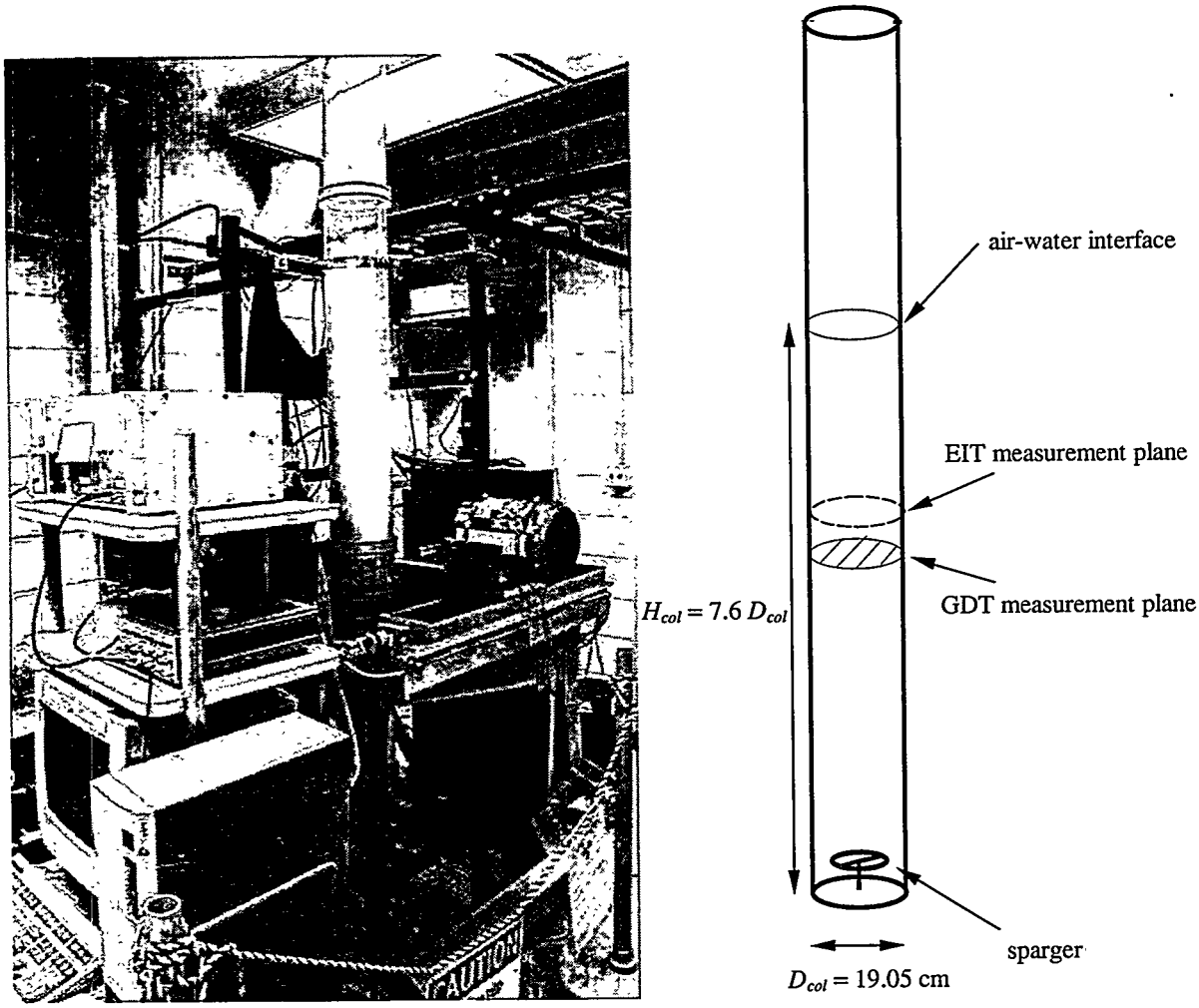

Figure 4.10. Experimental setup for EIT validation experiments in the Lexan bubble column. Left, a photograph of the EIT system connected to the strip electrode ring in the center of the column. The ^{137}Cs source and GDT traverse are visible on the right side of the photo. Right, a schematic diagram of the bubble column indicating measurement locations (not to scale).

schematically in Figure 4.10, has an inner diameter D_{col} of 19.05 cm, a wall thickness of 0.64 cm, and is built from interchangeable sections so that different diagnostic tools can be placed in the column. In this study, the EIT electrode section was placed near the center of the column. The 16 strip electrodes were centered on a plane $L = 97.16$ cm above the base, at a height-to-diameter ratio of $L/D_{col} = 5.1$. The column was filled with water to a depth H_{col} of 1.45 m, for a height-to-diameter ratio of 7.6; this depth placed the region of EIT sensitivity completely under water.

Dry air can be introduced at volumetric flow rates up to 600 L/min (superficial gas velocities up to 35 cm/s) through one of several interchangeable spargers at the base of the column. The spargers are electrically isolated to prevent interference with the EIT system. The

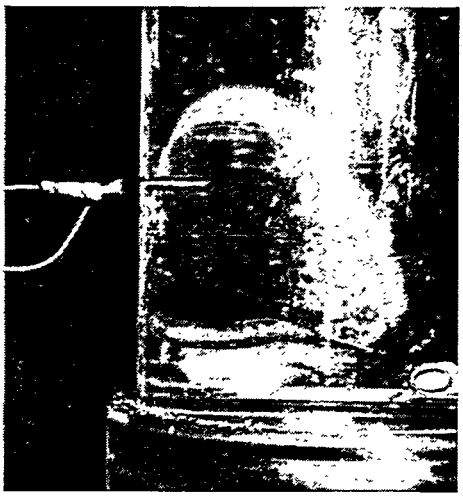

Figure 4.11. Typical cartridge heater used to maintain constant temperature within bubble-column flows.

column operates at ambient conditions, but the water is subject to evaporative cooling as air is bubbled through. To mitigate the effects of cooling on conductivity, heat energy was added to the flow by three cartridge heaters mounted at the column walls (Figure 4.11). A portable computer monitored the flow temperature via thermocouples mounted flush with the column walls, and the rate of heat addition was actively controlled by a rheostat to maintain a constant temperature in the flow. The liquid temperature was held constant by active heating to within ±0.2°C during experiments, which limited variations in conductivity with temperature to ±0.3%.

The goal for the gas-liquid tests was to validate EIT against GDT in a flow with variations on a larger scale than the solid-liquid flows. First, to investigate such a flow with smoothly varying properties, it was decided to create a homogeneous bubbly flow within the column, a flow in which bubbles do not coalesce and have minimal influence on one another's motion. Two different sparger designs for homogeneous flows (see Figure 4.12) were tested, and air was introduced at low superficial gas velocities ranging from 0.3 to 1.5 cm/s. Also, controlled amounts of electrolyte and Triton X-100 surfactant were added to the working liquid to reduce surface tension, prevent coalescence and delay the transition to churn-turbulent flow (*e.g.*, see Wilkinson *et al.*, 1992). Despite these efforts, a truly homogeneous bubbly flow could not be attained with either sparger. GDT reconstructions of the radial gas volume fraction profiles from both sparger designs were best described by fourth-order polynomials with maxima located at $r > 0$, instead of at the column centerline. Vortical motions were also observed at the higher flow rates, indicating a transition from homogeneous to churn-turbulent flow (George *et al.*, 1998b).

Consequently, a comparison of the two tomographic methods was made in churn-turbulent column flows. Such vertical flows normally have time-averaged volume fraction profiles that are approximately parabolic and can therefore be reconstructed by both the GDT and EIT algorithms. The sparger used to produce churn-turbulent flows is shown in Figure 4.13. This sparger is a hollow stainless steel toroid with a 10.16-cm centerline diameter, an inner tube diameter of 0.95 cm, and ten holes of diameter 0.16 cm facing downward. Spargers are often

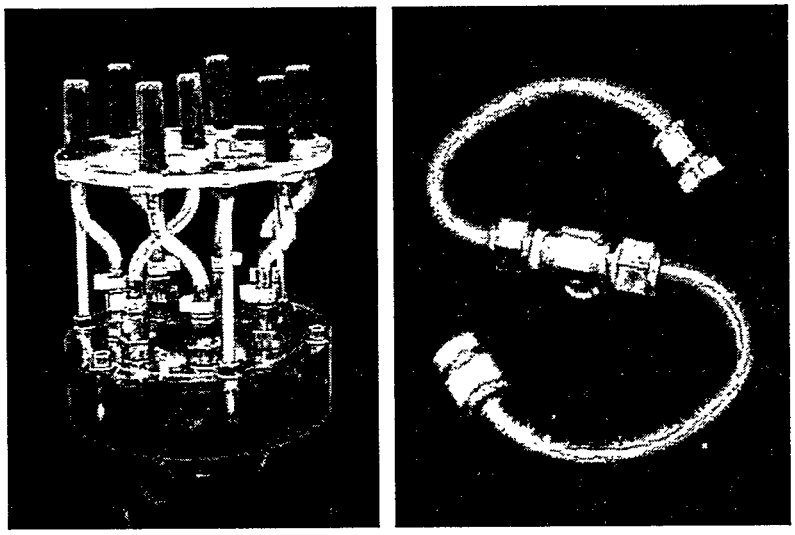

Figure 4.12. Sparger designs used in the unsuccessful homogeneous bubbly flow experiments. The sparger on the left injects air into the column through seven "airstone" frits made of sintered glass particles averaging 0.026 cm in diameter. The plenum and frit support are both 15.2 cm in diameter. The S-shaped sparger on the right is made of 0.95-cm I.D. copper tubing, and has an approximate diameter of 13 cm. Sixteen holes were drilled on each arm using a #80 (0.343 mm-diameter) drill bit.

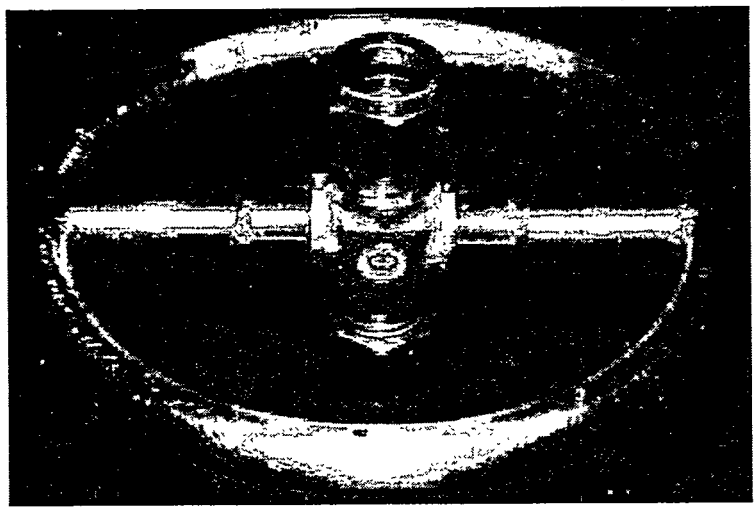

Figure 4.13. Ring sparger used in churn-turbulent flow experiments.

quantified by their porosity, the ratio of the total area of the sparger holes to the cross-sectional area of the column. In the Lexan bubble column, this sparger has a porosity of 0.00069.

Churn-turbulent experiments were performed using five air volumetric flow rates: Q_G = 25, 50, 75, 100 and 150 L/min. The corresponding superficial gas velocities U_G ranged from 1.5 to 8.8 cm/s. Figure 4.14 shows the conditions in the column for the minimum and maximum gas flow rates. At the lowest flow condition, a range of spherical and coalesced nonspherical bubble

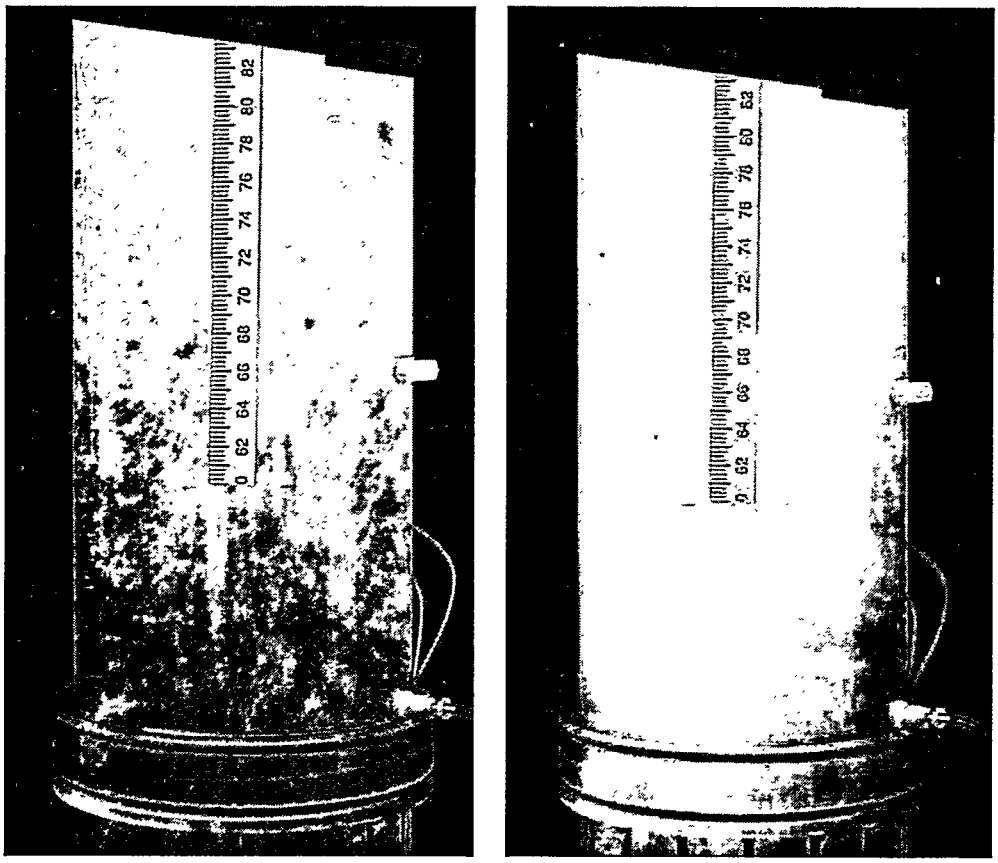

Figure 4.14. Churn-turbulent flow conditions in the transparent bubble column at minimum and maximum volumetric flow rates: (left) Q_G = 25 L/min, (right) Q_G = 150 L/min. The vertical scale is in centimeters.

sizes was evident, as was a central helical bubble stream. At rates of 75 L/min and above, the flow in the column was completely opaque and turbulent to the naked eye.

For each flow condition, 25 full EIT projection sets taken over a period of less than 20 seconds were averaged to obtain the voltage data for reconstructions. Multiple datasets were averaged to enable direct comparison with GDT results, which are inherently time-averaged, and to allow use of axisymmetric reconstruction algorithms. The conductivity of the water used in the gas-liquid experiments was 285±5 μS/cm. GDT measurements were taken in a plane 81.0 cm above the column floor (L/D_{col} = 4.25). This location, 16.2 cm below the center plane of the EIT electrodes, was chosen to avoid electrode obstruction of the photon paths. The GDT measurement chords were parallel and spaced 1 cm apart; detector counts were collected for 60 seconds along each chord.

In the EIT reconstructions, the three-dimensional code `EITAXI` was used with the assumption of a parabolic conductivity profile, given by Eq. 3.8 with $C_2 = 0$ (at this time, the quartic reconstruction option had not yet been added to `EITAXI`). Chord-averaged attenuation coefficients computed from GDT data were fit to a second or fourth-order polynomial before the Abel transform was taken. The choice of polynomial for each fit was made based upon the least-

squares error between the fit and the attenuation data. It should be noted that GDT reconstructions represent the phase distribution over a very thin, nearly two-dimensional cross section of the column, while EIT measures phase distributions within a three-dimensional volume extending above and below the electrode strips. However, with both the electrode center plane and GDT scan plane located well into the fully developed flow region ($L/D_{col} > 2$), variations in the phase distributions between the GDT and EIT measurement domains were expected to be negligible.

4.3.2. Initial Results

Figure 4.15 shows the gas volume profiles measured by both methods for all volumetric flow rates. The EIT profile tends to lie slightly above the GDT profile at each flow rate; however, the GDT and EIT gas volume fractions are in excellent agreement, falling within 0.01 of each other at all radial positions. Since the change in the local volume fraction across the column is as large as 0.20, this level of agreement strongly validates the EIT method. Values of the domain-averaged gas volume fraction $\bar{\varepsilon}_G$ were also determined from EIT and GDT by analytically averaging the profiles of Figure 4.15 over the column area. Figure 4.16 shows these cross-sectionally-averaged gas volume fractions as a function of superficial gas velocity U_G. Again, the GDT and EIT values are in very good agreement, differing by no more than 0.01 in $\bar{\varepsilon}_G$. This degree of consistency between GDT and EIT suggests that both methods are accurate for measuring axisymmetric profiles so long as temporal-averaging effects are benign.

4.3.3. Uncertainty Analysis

Because of the difference in collection times for the two methods (about 23 minutes for GDT but less than 20 seconds for EIT), it was decided to assess the effect of temporal averaging on the EIT and GDT reconstructions. Difficulties could arise, for example, from slow oscillations in the flows that could be averaged out by GDT but not by EIT. Separate flow measurements were taken under the same churn-turbulent flow conditions with an impedance-based bulk void fraction meter described in detail by Torczynski *et al.* (1997). This instrument has two rectangular electrodes 3.8 cm high, which subtend 120° each on opposite sides of the column (Figure 4.17). An impedance phase meter circuit operating at 50 kHz is used to excite the electrodes. In earlier work, this instrument was used to measure bulk gas volume fractions in the bubble column through comparisons of signals from flow and no-flow conditions. Here, the voltage across the electrodes was recorded with a Tektronix model TDS 640 digitizing oscilloscope for analysis of fluctuations in gas volume fraction. The meter is capable of detecting fluctuations with time scales on the order of 40 μs or longer. Since the time scales for churn-turbulent flows in the bubble column are expected to be much larger than this value, the meter was used to resolve temporal variations in the flow.

The voltage across the bulk meter electrodes was recorded over a period of ten minutes at each flow condition, and Fourier spectra were computed from the voltage data to determine the frequencies of gas volume fraction fluctuations. Signal spectra revealed no coherent periodic

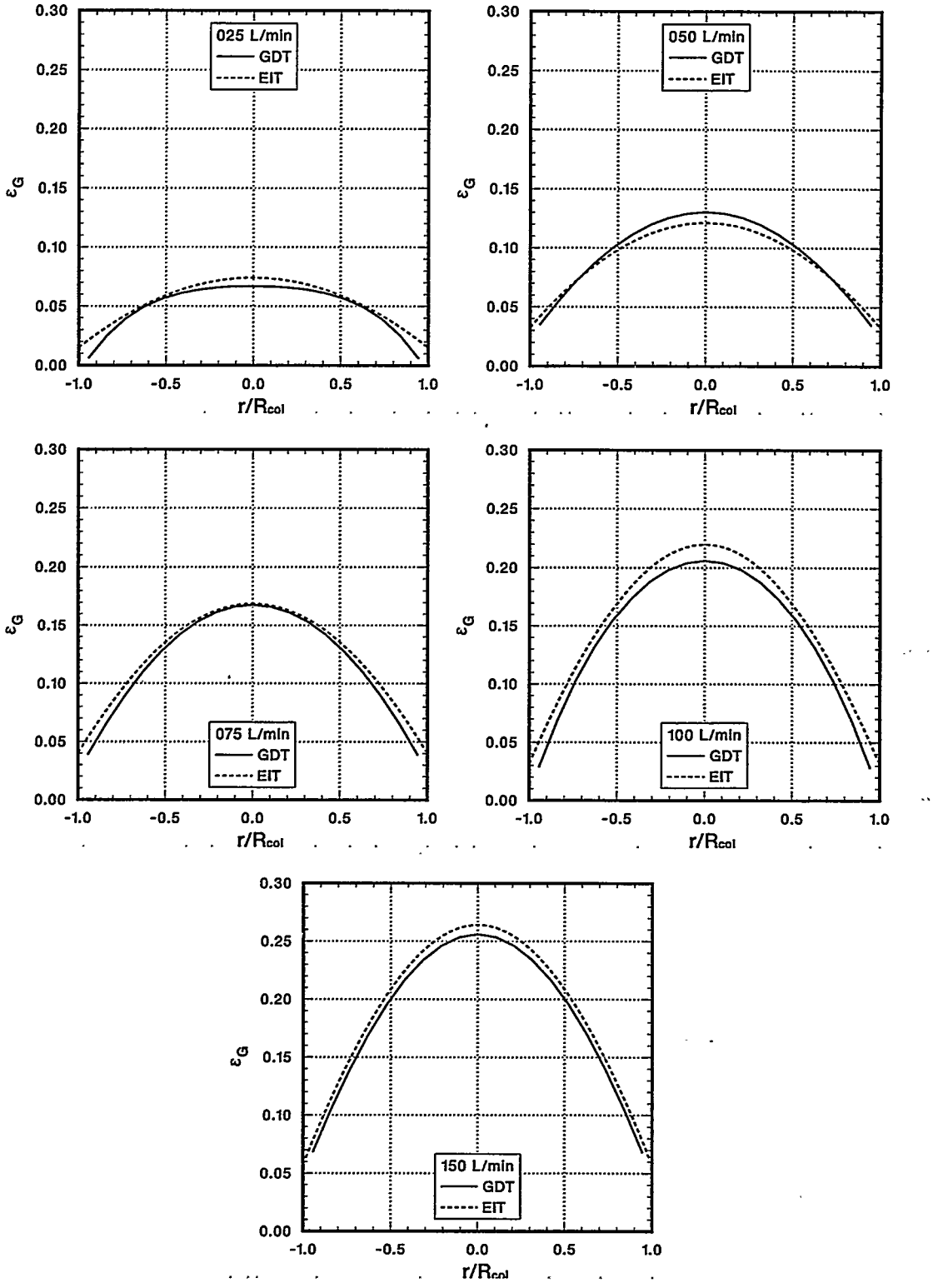

Figure 4.15. Comparisons of symmetric radial gas volume fraction profiles from GDT and EIT.

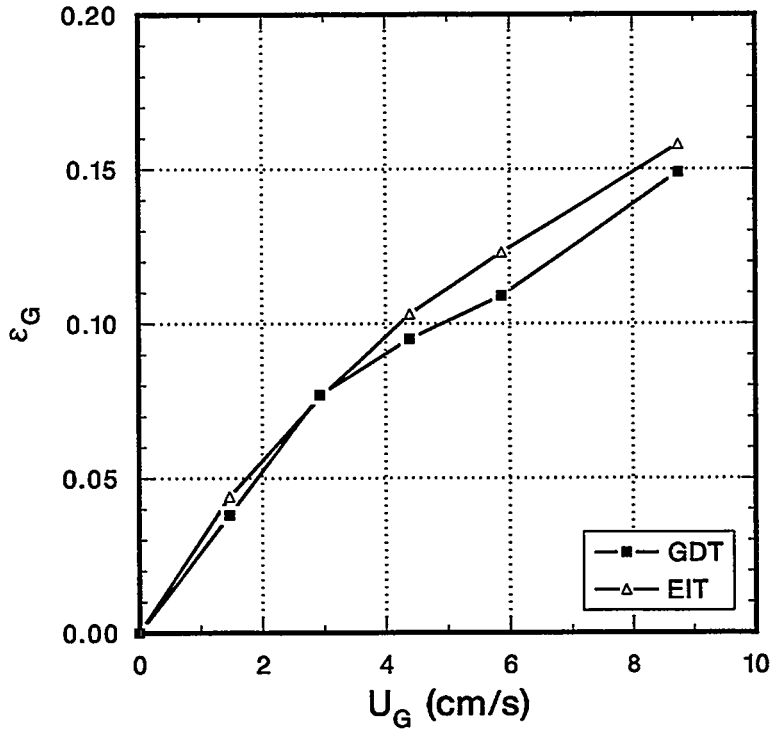

Figure 4.16. Comparison of cross-sectionally-averaged gas volume fractions measured by GDT and EIT.

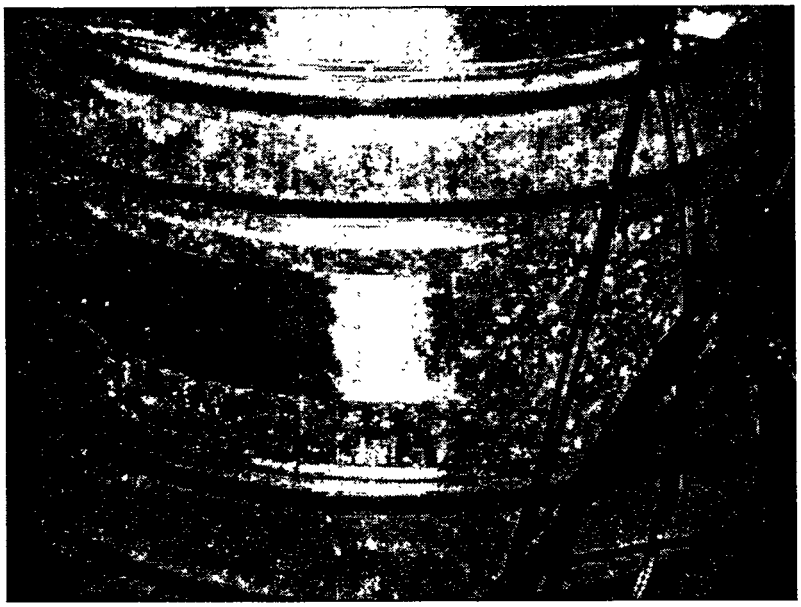

Figure 4.17. Impedance-based bulk void fraction meter used to investigate fluctuations in gas volume fraction.

flow behavior with a frequency less than 12.5 Hz; this alleviated the concern that EIT measurements were capturing data over only a portion of slow flow cycles. The bulk meter voltage signals were also analyzed to estimate the magnitude of variations in gas volume fraction

Table 4.1. Comparison of differences between EIT and GDT measurements with temporal fluctuations in gas volume fraction measured by the bulk void fraction meter.

U_G (cm/s)	$\bar{\varepsilon}_G^{EIT}$	$\langle \varepsilon_G \rangle^{GDT}$	$\bar{\varepsilon}_G^{EIT} - \langle \varepsilon_G \rangle^{GDT}$	$\Delta\bar{\varepsilon}_G^{Bulk}$
1.5	0.044	0.038	0.006	0.015
2.9	0.076	0.077	-0.001	0.016
4.4	0.103	0.095	0.008	0.018
5.9	0.123	0.109	0.014	0.020
8.8	0.158	0.149	0.009	0.023

for all flow conditions. Using a sum-of-squares method, the rms voltage variation measured without gas flow was subtracted from the rms variation at each flow condition to estimate variations in the signals due solely to variations in gas volume fraction. Time-averaged voltages $\bar{V}$ were correlated with cross-sectionally-averaged gas volume fractions $\langle \varepsilon_G \rangle^{GDT}$ determined from concurrent GDT scans, and temporal variations in $\bar{\varepsilon}_G^{Bulk}$ at each flow condition were estimated from the voltage variations and the correlation of $\langle \varepsilon_G \rangle^{GDT}$ versus $\bar{V}$.

Table 4.1 compares $\Delta\bar{\varepsilon}_G^{Bulk}$, the estimate of these temporal variations, with $\bar{\varepsilon}_G^{EIT} - \langle \varepsilon_G \rangle^{GDT}$, the difference between the average values measured by EIT and GDT. Since $\Delta\bar{\varepsilon}_G^{Bulk}$ and $\bar{\varepsilon}_G^{EIT} - \langle \varepsilon_G \rangle^{GDT}$ are comparable, the different methods of temporal averaging by EIT and GDT may account for some of the difference between the average values measured by these two techniques. However, since the difference $\bar{\varepsilon}_G^{EIT} - \langle \varepsilon_G \rangle^{GDT}$ and the variation $\Delta\bar{\varepsilon}_G^{Bulk}$ are small compared to both $\bar{\varepsilon}_G^{EIT}$ and $\langle \varepsilon_G \rangle^{GDT}$, both methods of temporal averaging appear to be benign. The relatively small difference between the methods may also be taken as evidence that the difference in measurement domains (negligible vertical thickness for GDT versus a few diameters in the vertical direction for EIT) is also benign. These conclusions are probably valid only for the fully developed flow region; it is likely that the different temporal averaging methods and measurement domains would be more important for strongly developing flows. Future investigations will examine the effects of temporal averaging by EIT and GDT more closely.

4.3.4. Modified Maxwell-Hewitt Relation and Revised Results

Another possible explanation for the difference in results between GDT and EIT, one related to the issue of temporal averaging, is the small but finite vertical motion of bubbles during EIT measurements. One assumption inherent in EIT reconstructions is that the impedance distribution in the domain does not change significantly over the course of voltage measurements (Ceccio and George, 1996). Any movement or change in shape of an insulating void over the course of a projection set will yield inconsistent voltages that may produce a conductivity reconstruction "smeared" over time. While the three-dimensional Maxwell-Hewitt relation (Eq. 3.13) assumes three-dimensional insulating inclusions in the domain (*e.g.*, spherical

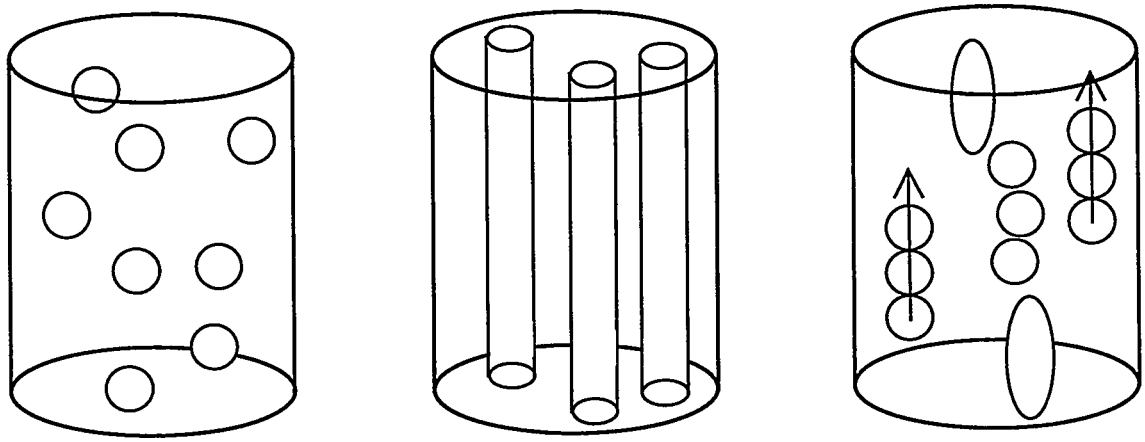

Figure 4.18. Concept of the modified Maxwell-Hewitt relation. Left, spherical insulators in a three-dimensional reconstruction; center, cylindrical insulators in a two-dimensional reconstruction; right, "time-exposure" of moving and deformed bubbles in a realistic bubble-column flow.

bubbles), the two-dimensional version (Eq. 3.14) assumes invariance in the axial direction, and the domain it describes may be thought of as infinitely high and containing cylindrical objects of infinite height (Figure 4.18). Vertical motion or axial elongation of bubbles during voltage acquisitions in the column may produce an effective conductivity distribution somewhere between the ideal three-dimensional and two-dimensional cases, so that Eq. 3.13 is not strictly applicable. (Recall that the electric fields in the column are three-dimensional, although the reconstructed distribution is two-dimensional.) Since the only difference between the two Maxwell-Hewitt relations is the factor of ½ versus 1 in the denominator, adjustment of this factor to a value between ½ and 1 could approximately account for this axial motion of the gas phase during EIT measurements.

At the same time the EIT reconstruction algorithm was modified to include quartic conductivity profiles, empirical tests were conducted to find a value of the Maxwell-Hewitt coefficient that further improved agreement between EIT and GDT. Figure 4.19 shows GDT and EIT reconstructions of the gas volume fraction profile from a preliminary test using both quadratic and quartic profiles for the gamma attenuation and the electrical conductivity. The top plot is a comparison when the electrical conductivity is converted into gas volume fraction using the original Maxwell-Hewitt relation. Agreement is acceptable, although the EIT values are always somewhat greater than the GDT values. The bottom plot is a comparison when Eq. 3.13 is modified in the following manner:

$$\varepsilon_G(r) = 1 - \varepsilon_L(r) = \frac{1 - [\sigma(r)/\sigma_L]}{1 + \frac{3}{5}[\sigma(r)/\sigma_L]} \text{ (modified Maxwell-Hewitt).} \qquad (4.4)$$

The value of ⅗ for the Maxwell-Hewitt coefficient is reasonable, based on the discussion above and the study of the accuracy of the Maxwell-Hewitt relation in Chapter 3. The agreement

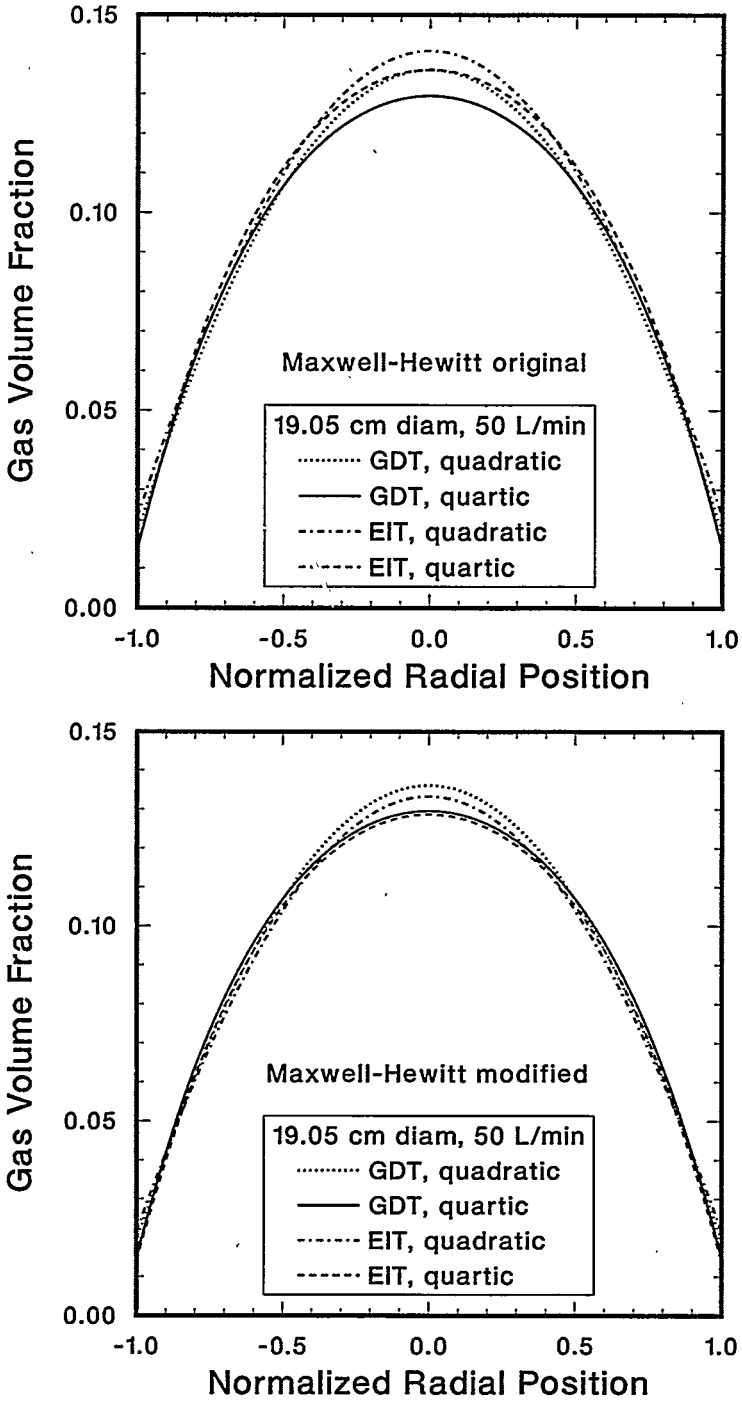

Figure 4.19. GDT and EIT reconstructions using quadratic and quartic profiles. Top, original Maxwell-Hewitt relation; bottom, modified Maxwell-Hewitt relation.

between GDT and EIT is substantially improved with the application of Eq. 4.4 to EIT reconstruction. Although no systematic study has yet been performed, spot checks on several other cases appear to indicate a similar improvement between GDT and EIT gas volume fraction profiles. This will be a topic of future EIT investigations.